

---

# PLUG-AND-PLAY EXTERNAL AND INTERNAL PRIORS FOR IMAGE RESTORATION

---

**Pasquale Cascarano**

Department of Mathematics  
University of Bologna, 40126, Bologna, Italy  
pasquale.cascarano2@unibo.it

**Elena Loli Piccolomini**

Department of Computer Science and Engineering  
University of Bologna, 40126, Bologna, Italy  
elena.loli@unibo.it

**Elena Morotti**

Department of Computer Science and Engineering  
University of Bologna, 40126, Bologna, Italy  
elena.morotti4@unibo.it

**Andrea Sebastiani**

Department of Mathematics  
University of Bologna, 40126, Bologna, Italy  
andrea.sebastiani3@unibo.it

## ABSTRACT

Image restoration problems were traditionally formulated as the minimization of variational models, including data-fidelity and regularization terms, performed by optimization methods with well-established convergence properties. Recently, Plug-and-Play (PnP) methods for image restoration have obtained very good results and popularity by introducing, in iterative proximal algorithms, any off-the-shelf denoiser as priors.

Deep Convolutional Neural Network (CNN) denoisers specify *external priors* (related to an outer training set) which well reflect image statistics; however they fail when dealing with unseen noise variance and image patterns in the given image. Conversely, the so-called internal denoisers induce *internal priors* tailored on the observed data, by forcing specific features on the desired image. We propose a new PnP scheme, based on the Half-Quadratic Splitting proximal algorithm, combining external and internal priors. Moreover, differently from other existing PnP methods, we propose a deep denoiser acting on the image gradient domain. Finally, we prove that a fixed point convergence is guaranteed for the proposed scheme under suitable conditions. In the experimental part, we use CNN denoisers and the Total Variation functional specifying external and internal priors, respectively. We prove the effectiveness of the proposed method in restoring blurred noisy images, both in simulated and real medical settings.

## 1 Introduction

In the field of computational imaging, Image Restoration (IR) aims at recovering an unknown clean image from its noisy, blurred and/or undersampled measurement. Mathematically, by lexicographically reordering the images as vectors, a generic IR task can be written as the following inverse problem:

$$\text{Find } \mathbf{u} \text{ such that } \mathbf{v} = \mathbf{A}\mathbf{u} + \mathbf{e}, \quad (1)$$

where  $\mathbf{v} \in \mathbb{R}^m$  is the given image,  $\mathbf{u} \in \mathbb{R}^n$  is the unknown desired image and  $\mathbf{A} \in \mathbb{R}^{m \times n}$  is the forward linear operator defining the IR specific task (we suppose here the images are reordered as one-dimensional vectors). The observed image  $\mathbf{v}$  is usually affected by noise  $\mathbf{e} \in \mathbb{R}^m$ , which we assume in this work as Additive White Gaussian Noise (AWGN).

In general, IR problems as (1) are well-known to be ill-posed, meaning that the properties of existence, uniqueness and/or stability of the desired solution  $\mathbf{u}$  are not all guaranteed [2]. Hence, model-based reconstruction methods attempt to find a good estimate  $\mathbf{u}^* \in \mathbb{R}^n$  of the unknown  $\mathbf{u}$  as the solution of a minimization problem whose objective function is the sum of two terms  $f$  and  $g$ , namely:

$$\mathbf{u}^* \in \arg \min_{\mathbf{u} \in \mathbb{R}^n} \{f(\mathbf{u}) + g(\mathbf{u})\}. \quad (2)$$

The functions  $f$  and  $g$  are usually referred to as *data fidelity* and *regularization* terms, respectively. The former is a task-related term which models the noise affecting the starting measurement  $\mathbf{v}$ , whereas the latter induces prior information on the estimate  $\mathbf{u}^*$  by reflecting, for example, sparsity patterns, smoothness or geometric assumptions. Often,  $f$  is set as an  $L_p$ -norm based function measuring the residual between  $\mathbf{A}\mathbf{u}$  and  $\mathbf{v}$ , with  $p$  strictly related to noise statistics. It is well-known that a squared  $L_2$ -norm fidelity fits with the previous assumption of AWGN affecting the measurement  $\mathbf{v}$ .

The choice of a regularizer is a challenging task. In a model-based approach, a widely used strategy is to define  $g$  as a handcrafted term, based on desired properties of the reconstructed image in a specific domain, such as the gradient or the wavelet domain. For this reason we say that handcrafted regularizers induce an image-specific prior on  $\mathbf{u}^*$ .

The advent of learning-based methods, their outstanding performances together with the availability of large datasets and the development of free online platforms to run the algorithms, have moved the researchers interest towards these new tools in image processing applications. The main drawback of learning-based algorithms is the lack of solid mathematical foundations and their strong dependence on the given set of examples used in the training phase which may limit their usage. However, we believe that a new frontier in the image processing field is represented by the Plug-and-Play (PnP) framework, firstly proposed in [27], which is a very interesting tool keeping convergence properties while using learning strategies. In [27] the authors strikingly showed that a closed-form regularizer is not always the best possible choice to properly induce prior information on the desired solution. Technically, the PnP approach derives from the iterative scheme of proximal algorithms, applied to solve regularized optimization problems as (2), where the resulting modular structure allows to deal with the data fidelity  $f$  and the regularization term  $g$ , separately. Since the regularizer-related sub-step reads as a denoising task, the authors have replaced it with any off-the-shelf denoiser, so that the computed solution inherits prior information not necessarily deriving from a closed-form regularization term.

So far, a large number of papers on PnP have been published focusing on different aspects of the scheme, such as the proximal algorithm or the denoiser employed. Different proximal algorithms are considered: the Alternating Direction Method of Multipliers (ADMM) in [27, 24, 26], the primal-dual in [21], the Half-Quadratic Splitting (HQS) in [32, 33, 31], the Fast Iterative Shrinkage-Thresholding Algorithm (FISTA) in [11] and even stochastic Forward-Backward Splitting method (FBS) [25]. Several denoisers have been successfully plugged in the previous iterative schemes. They are usually labelled as internal or external denoisers. Internal denoisers, such as the proximal maps of handcrafted regularizers, the BM3D [8] and the Non-Local Mean (NLM) filter [3], specify *internal priors* to definite features of the desired image. External denoisers, such as Gaussian Mixture Models (GMMs) [34] and trained nonlinear reaction diffusion based denoisers [6] induce *external priors* related to an outer set of clean images [19]. Nowadays, modelling a prior based on deep learning techniques can lead to outstanding performances in many IR problems, as shown in [14, 15], and these data-driven strategies have reached the state-of-the-art in denoising [29, 4]. For this reason, in [32, 31, 17] the authors have proposed to combine the PnP framework with learning-based external priors specified through pre-trained Convolutional Neural Network (CNN) denoisers.

Concerning theoretical results, since not all the plugged denoisers are proximal maps of regularization terms [5], the PnP schemes lack of classical variational interpretability and this makes difficult a detailed convergence analysis. To the best of our knowledge, only few works have already addressed the PnP convergence issue. In [24] the authors have shown that if the plugged denoiser satisfies symmetric gradient and nonexpansiveness properties then the ADMM-based PnP scheme converges to the minimum of an implicit defined regularized objective function. Under the weaker assumption of bounded denoisers, in [5] a fixed-point convergence for the PnP, relying on ADMM, has been addressed. Moreover, it has been proved a fixed-point convergence theorem for a PnP ADMM framework, assuming that learned denoisers are trained with a variant of spectral normalization in order to guarantee a constrained Lipschitz constant [23]. Finally, in [17] the authors have shown that PnP frameworks based on different proximal algorithms share the same fixed-point under the assumption of continuous denoisers.

## Motivation and contributions of the paper

Learning-based denoisers rely on the external training set more than on the image to be restored, so they can fail when dealing with unseen noise variance and image patterns. Conversely, internal denoisers are tailored to the observed data but they struggle to deal with several different image features simultaneously. Motivated by the apparent complementarity of external and internal priors and the effectiveness of combining internal and external denoisers, as also observed in [19], here we propose a new hybrid PnP framework, which relies on the Half-Quadratic Splitting algorithm and uses a CNN-based and a handcrafted denoiser.

In all the previous works focusing on deep learning based PnP frameworks, the external denoiser acts on the computed image ([32, 31] only to cite some examples). Since it is well-known that a prior defined on the gradient image domain

may enhance image reconstructions both in terms of shape recovering and noise removal, we propose here to specify a gradient-based external prior through CNN networks trained on the noisy image gradients.

Moreover, under general conditions on both the external and internal denoisers, we prove a fixed-point convergence theorem for the proposed scheme.

In the experimental part, we choose as denoiser, specifying an internal prior, the widely used Total Variation (TV) [22] which is largely employed in different imaging applications, such as medical imaging [12, 13], for its good behaviour in removing noise and preserving curved contours of the objects. We apply the proposed hybrid PnP method to restore blurred and noisy images. We test our framework by considering the results obtained by using both external and internal priors and we show the improvement with respect to the use of only one of them. Concerning the comparison with other methods, we limit to the one proposed in [32], since the authors show that their algorithm outperforms the state-of-the-art deblurring-and-denoising methods. The numerical tests, performed on synthetic piecewise constant and real medical images, provide very high quality reconstructions and confirm the robustness of the framework in both restoring low contrasted objects with different shapes and in removing noise.

## Organization of the paper

In this paper, we first present a general hybrid PnP framework using the HQS as proximal algorithm (Section 2) and we prove the fixed-point convergence theorem in the broad case of plugging both an external and an internal denoiser (Section 3). Then, we focus in Section 4 on the particular choices of the denoisers implemented to perform the numerical tests reported in Section 5.

## 2 Hybrid Plug-and-Play HQS method

Before introducing the proposed PnP scheme we show how to apply the HQS framework to solve the optimization problem (2) for the following choice of  $f$  and  $g$ .

Due to the previous assumption of AWGN affecting the measurement  $\mathbf{v}$ , we fix the fidelity term as  $f(\mathbf{u}) := \frac{1}{2} \|\mathbf{A}\mathbf{u} - \mathbf{v}\|_2^2$ .

We now consider the regularizer  $g$  as the combination of two different terms as:

$$g(\mathbf{u}) := \lambda g_1(\mathbf{L}_1 \mathbf{u}) + \eta g_2(\mathbf{L}_2 \mathbf{u}), \quad (3)$$

where  $g_1$  and  $g_2$  are positive and convex real-valued maps:

$$g_1 : \mathbb{R}^{l_1} \rightarrow \mathbb{R}^+, \quad g_2 : \mathbb{R}^{l_2} \rightarrow \mathbb{R}^+, \quad (4)$$

with  $l_1$  and  $l_2$  positive integers,  $\mathbf{L}_1 \in \mathbb{R}^{l_1 \times n}$  and  $\mathbf{L}_2 \in \mathbb{R}^{l_2 \times n}$ . The parameters  $\lambda$  and  $\eta$  are non-negative constants weighting the contribution of  $g_1$  and  $g_2$ , respectively.

By the previous assumptions the problem (2) can be conceived as finding an estimate  $\mathbf{u}^*$  so that:

$$\mathbf{u}^* \in \arg \min_{\mathbf{u} \in \mathbb{R}^n} \left\{ \frac{1}{2} \|\mathbf{A}\mathbf{u} - \mathbf{v}\|_2^2 + \lambda g_1(\mathbf{L}_1 \mathbf{u}) + \eta g_2(\mathbf{L}_2 \mathbf{u}) \right\}. \quad (5)$$

We consider the HQS iterative method described in [9, 28] as numerical solver to compute  $\mathbf{u}^*$ . By introducing the auxiliary variables  $\mathbf{t}$  and  $\mathbf{z}$  so as  $\mathbf{t} := \mathbf{L}_1 \mathbf{u}$  and  $\mathbf{z} := \mathbf{L}_2 \mathbf{u}$ , the following penalized half-quadratic function is taken into account:

$$\mathcal{L}(\mathbf{u}, \mathbf{t}, \mathbf{z}; \rho^{\mathbf{t}}, \rho^{\mathbf{z}}) = \frac{1}{2} \|\mathbf{A}\mathbf{u} - \mathbf{v}\|_2^2 + \lambda g_1(\mathbf{t}) + \eta g_2(\mathbf{z}) + \frac{\rho^{\mathbf{t}}}{2} \|\mathbf{L}_1 \mathbf{u} - \mathbf{t}\|_2^2 + \frac{\rho^{\mathbf{z}}}{2} \|\mathbf{L}_2 \mathbf{u} - \mathbf{z}\|_2^2. \quad (6)$$

At each iteration  $k$ , the HQS algorithm performs this alternated minimization scheme with respect to  $\mathbf{t}$ ,  $\mathbf{z}$  and the primal variable  $\mathbf{u}$ :

$$\begin{cases} \mathbf{t}_{k+1} \in \arg \min_{\mathbf{t} \in \mathbb{R}^{l_1}} \left\{ \lambda g_1(\mathbf{t}) + \frac{\rho_k^{\mathbf{t}}}{2} \|\mathbf{L}_1 \mathbf{u}_k - \mathbf{t}\|_2^2 \right\} \end{cases} \quad (7)$$

$$\begin{cases} \mathbf{z}_{k+1} \in \arg \min_{\mathbf{z} \in \mathbb{R}^{l_2}} \left\{ \eta g_2(\mathbf{z}) + \frac{\rho_k^{\mathbf{z}}}{2} \|\mathbf{L}_2 \mathbf{u}_k - \mathbf{z}\|_2^2 \right\} \end{cases} \quad (8)$$

$$\begin{cases} \mathbf{u}_{k+1} = \arg \min_{\mathbf{u} \in \mathbb{R}^n} \left\{ \frac{1}{2} \|\mathbf{A} \mathbf{u} - \mathbf{v}\|_2^2 + \frac{\rho_k^{\mathbf{t}}}{2} \|\mathbf{L}_1 \mathbf{u} - \mathbf{t}_{k+1}\|_2^2 + \frac{\rho_k^{\mathbf{z}}}{2} \|\mathbf{L}_2 \mathbf{u} - \mathbf{z}_{k+1}\|_2^2 \right\} \end{cases} \quad (9)$$

where  $(\rho_k^{\mathbf{t}})_{k=1}^{\infty}$  and  $(\rho_k^{\mathbf{z}})_{k=1}^{\infty}$  are chosen as two non-decreasing sequences of positive penalty parameters.

---

**Algorithm 1** General HQS

---

**Input:**  $\lambda, \eta$  and  $(\rho_k^{\mathbf{t}})_{k=1}^{\infty}, (\rho_k^{\mathbf{z}})_{k=1}^{\infty}, \mathbf{A}, \mathbf{L}_1, \mathbf{L}_2, \mathbf{v}, \mathbf{u}^1$ ,

**while** Not Converge **do**

$$\mathbf{t}_{k+1} = \text{prox}_{g_1, \frac{\lambda}{\rho_k^{\mathbf{t}}}}(\mathbf{L}_1 \mathbf{u}_k)$$

$$\mathbf{z}_{k+1} = \text{prox}_{g_2, \frac{\eta}{\rho_k^{\mathbf{z}}}}(\mathbf{L}_2 \mathbf{u}_k)$$

$$\mathbf{u}_{k+1} = \arg \min_{\mathbf{u} \in \mathbb{R}^n} \left\{ \frac{1}{2} \|\mathbf{A} \mathbf{u} - \mathbf{v}\|_2^2 + \frac{\rho_k^{\mathbf{t}}}{2} \|\mathbf{L}_1 \mathbf{u} - \mathbf{t}_{k+1}\|_2^2 + \frac{\rho_k^{\mathbf{z}}}{2} \|\mathbf{L}_2 \mathbf{u} - \mathbf{z}_{k+1}\|_2^2 \right\}$$

**end while**

---

A pseudocode of the HQS method for the numerical solution of the optimization problem in (5) is shown in Algorithm 1. We remark that under particular conditions, such as the convexity of  $g_1$  and  $g_2$ , the sequence  $(\mathbf{u}_k)_{k=1}^{\infty}$  computed in Algorithm 1 converges to a global minimum of (5) [9, 28, 20].

The key feature of HQS is that the prior related sub-steps (7) and (8) are specified through the proximal maps of  $g_1$  and  $g_2$ , respectively, which are mathematically equivalent to regularized denoising problems. The PnP frameworks exploit both this equivalence and the modular structure of the algorithm by replacing such proximal maps with any off-the-shelf denoiser.

Now we present the proposed hybrid PnP scheme. We introduce a pre-trained learning-based denoiser  $\mathcal{D}_{\sigma}^{\text{ext}}$  and an image-specific denoiser  $\mathcal{D}_{\gamma}^{\text{int}}$  depending on the positive parameters  $\sigma$  and  $\gamma$  related to the noise-level in the images to be denoised, so that the greater are  $\sigma$  and  $\gamma$ , the more powerful is the denoising realized. In particular, in our scheme we choose two sequences  $(\sigma_k)_{k=1}^{+\infty}$  and  $(\gamma_k)_{k=1}^{+\infty}$  such that, at step  $k$ ,  $\mathcal{D}_{\sigma_k}^{\text{ext}}$  and  $\mathcal{D}_{\gamma_k}^{\text{int}}$  replace the sub-steps (7) and (8), respectively. A standard assumption in PnP is that  $\sigma_k$  and  $\gamma_k$  are both related with the penalty parameters  $\rho_k^{\mathbf{t}}$  and  $\rho_k^{\mathbf{z}}$  through these formulas:

$$\sigma_k := \sqrt{\frac{\alpha}{\rho_k^{\mathbf{t}}}}, \quad \gamma_k := \sqrt{\frac{\beta}{\rho_k^{\mathbf{z}}}}, \quad (10)$$

where  $\alpha$  and  $\beta$  are positive scaling factors.

A sketch of the resulting hybrid PnP framework is reported in Algorithm 2.

---

**Algorithm 2** Hybrid PnP

---

**Input:**  $\alpha, \beta$  and  $(\rho_k^{\mathbf{t}})_{k=1}^{\infty}, (\rho_k^{\mathbf{z}})_{k=1}^{\infty}, \mathbf{A}, \mathbf{L}_1, \mathbf{L}_2, \mathbf{v}, \mathbf{u}^1$

**while** Not Converge **do**

$$\mathbf{t}_{k+1} = \mathcal{D}_{\sigma_k}^{\text{ext}}(\mathbf{L}_1 \mathbf{u}_k)$$

$$\mathbf{z}_{k+1} = \mathcal{D}_{\gamma_k}^{\text{int}}(\mathbf{L}_2 \mathbf{u}_k)$$

$$\mathbf{u}_{k+1} = \arg \min_{\mathbf{u} \in \mathbb{R}^n} \left\{ \frac{1}{2} \|\mathbf{A} \mathbf{u} - \mathbf{v}\|_2^2 + \frac{\rho_k^{\mathbf{t}}}{2} \|\mathbf{L}_1 \mathbf{u} - \mathbf{t}_{k+1}\|_2^2 + \frac{\rho_k^{\mathbf{z}}}{2} \|\mathbf{L}_2 \mathbf{u} - \mathbf{z}_{k+1}\|_2^2 \right\}$$

**end while**

---

### 3 Convergence results of Plug-and-Play HQS methods

To analyze the convergence properties of Algorithm 2, we start observing that if the denoisers  $\mathcal{D}_{\sigma}^{\text{ext}}$  and  $\mathcal{D}_{\gamma}^{\text{int}}$  are the proximal maps of two convex functions  $g_1$  and  $g_2$ , respectively, then the convergence to a global minimum of the objective function in (5) is guaranteed [9, 28]. However, in [24] the authors observe that a denoiser is a proximal map

when it is nonexpansive with symmetric gradient, thus limiting the set of suitable denoisers. In the effort of allowing less strict conditions on the involved denoisers, we show in this section that the proposed Algorithm 2 satisfies a fixed-point convergence theorem provided only their boundedness.

**Definition 3.1** (Bounded Denoiser [5]). A *bounded denoiser* is a function  $\mathcal{D}_\epsilon : \mathbb{R}^l \rightarrow \mathbb{R}^l$  such that for any  $\mathbf{t} \in \mathbb{R}^l$  and  $\epsilon \in \mathbb{R}^+$  the following inequality holds:

$$\|\mathcal{D}_\epsilon(\mathbf{t}) - \mathbf{t}\|_2^2 \leq \epsilon^2 C_{\mathcal{D}} \quad (11)$$

for a constant  $C_{\mathcal{D}}$  independent of  $\epsilon$ .

The previous definition entails that given the sequence  $(\epsilon_k)_{k=1}^{+\infty}$ ,  $\mathcal{D}_{\epsilon_k}$  converges to the identity function of  $\mathbb{R}^l$  as  $\epsilon_k \rightarrow 0$ .

In order to state and prove the following fixed-point theorem, we make some assumptions.

Given  $(\rho_k^{\mathbf{t}})_{k=1}^{\infty}$  and  $(\rho_k^{\mathbf{z}})_{k=1}^{\infty}$  non-decreasing positive sequences,  $\mathbf{L}_1 \in \mathbb{R}^{l_1 \times n}$ ,  $\mathbf{L}_2 \in \mathbb{R}^{l_2 \times n}$  as input for Algorithm 2, then we assume:

**A.1**  $\mathcal{D}_{\sigma_k}^{\text{ext}}$  and  $\mathcal{D}_{\gamma_k}^{\text{int}}$  are bounded denoisers.

**A.2**  $\mathbf{L}_1$  and  $\mathbf{L}_2$  are full-rank matrices.

**A.3**  $\sum_{k=1}^{+\infty} \sqrt{\frac{k}{\rho_k^{\mathbf{z}}}} < +\infty$ ,  $\sum_{k=1}^{+\infty} \sqrt{\frac{k}{\rho_k^{\mathbf{t}}}} < +\infty$  and  $\frac{\rho_k^{\mathbf{z}}}{\rho_k^{\mathbf{t}}} \rightarrow c$  where  $c \in \mathbb{R}^+$ .

**Theorem 3.1** (Fixed-point convergence theorem for the hybrid PnP algorithm). *Given the assumptions A.1-A.3, there exist  $\mathbf{t}^* \in \mathbb{R}^{l_1}$ ,  $\mathbf{z}^* \in \mathbb{R}^{l_2}$  and  $\mathbf{u}^* \in \mathbb{R}^n$  such that, for  $k \rightarrow \infty$ , the following relations hold:*

$$\mathbf{t}_k \rightarrow \mathbf{t}^*, \quad \mathbf{L}_1 \mathbf{u}_k \rightarrow \mathbf{t}^*, \quad \mathbf{z}_k \rightarrow \mathbf{z}^*, \quad \mathbf{L}_2 \mathbf{u}_k \rightarrow \mathbf{z}^*, \quad \mathbf{u}_k \rightarrow \mathbf{u}^*,$$

where  $\mathbf{t}_k, \mathbf{z}_k, \mathbf{u}_k$  are computed as in Algorithm 2 at step  $k$ .

*Proof.* By observing that  $\mathbf{u}_{k+1}$  is the optimal solution of the minimization problem (9), and by using the relations in (10) and the assumption **A.1**, we get the following chain of inequalities:

$$\begin{aligned} & \frac{1}{2} \|\mathbf{A} \mathbf{u}_{k+1} - \mathbf{v}\|_2^2 + \frac{\rho_k^{\mathbf{t}}}{2} \|\mathbf{t}_{k+1} - \mathbf{L}_1 \mathbf{u}_{k+1}\|_2^2 + \frac{\rho_k^{\mathbf{z}}}{2} \|\mathbf{z}_{k+1} - \mathbf{L}_2 \mathbf{u}_{k+1}\|_2^2 \leq \\ & \leq \frac{1}{2} \|\mathbf{A} \mathbf{u}_k - \mathbf{v}\|_2^2 + \frac{\rho_k^{\mathbf{t}}}{2} \|\mathbf{t}_{k+1} - \mathbf{L}_1 \mathbf{u}_k\|_2^2 + \frac{\rho_k^{\mathbf{z}}}{2} \|\mathbf{z}_{k+1} - \mathbf{L}_2 \mathbf{u}_k\|_2^2 = \\ & = \frac{1}{2} \|\mathbf{A} \mathbf{u}_k - \mathbf{v}\|_2^2 + \frac{\rho_k^{\mathbf{t}}}{2} \|\mathcal{D}_{\sigma_k}^{\text{ext}}(\mathbf{L}_1 \mathbf{u}_k) - \mathbf{L}_1 \mathbf{u}_k\|_2^2 + \frac{\rho_k^{\mathbf{z}}}{2} \|\mathcal{D}_{\gamma_k}^{\text{int}}(\mathbf{L}_2 \mathbf{u}_k) - \mathbf{L}_2 \mathbf{u}_k\|_2^2 \leq \\ & \leq \frac{1}{2} \|\mathbf{A} \mathbf{u}_k - \mathbf{v}\|_2^2 + \frac{\rho_k^{\mathbf{t}}}{2} \sigma_k^2 C_{\mathcal{D}^{\text{ext}}} + \frac{\rho_k^{\mathbf{z}}}{2} \gamma_k^2 C_{\mathcal{D}^{\text{int}}} = \\ & = \frac{1}{2} \|\mathbf{A} \mathbf{u}_k - \mathbf{v}\|_2^2 + \frac{\alpha}{2} C_{\mathcal{D}^{\text{ext}}} + \frac{\beta}{2} C_{\mathcal{D}^{\text{int}}} \leq \\ & = \frac{1}{2} \|\mathbf{A} \mathbf{u}_k - \mathbf{v}\|_2^2 + \tilde{C}, \end{aligned} \quad (12)$$

with  $\tilde{C} := \frac{\alpha}{2} C_{\mathcal{D}^{\text{ext}}} + \frac{\beta}{2} C_{\mathcal{D}^{\text{int}}}$ .

Since all the considered terms in (12) are positive, the following inequalities hold:

$$\frac{1}{2} \|\mathbf{A} \mathbf{u}_{k+1} - \mathbf{v}\|_2^2 \leq \frac{1}{2} \|\mathbf{A} \mathbf{u}_k - \mathbf{v}\|_2^2 + \tilde{C} \leq \dots \leq \frac{1}{2} \|\mathbf{A} \mathbf{u}_1 - \mathbf{v}\|_2^2 + k\tilde{C}. \quad (13)$$

For the same reason, using (12) and (13) we get:

$$\|\mathbf{t}_{k+1} - \mathbf{L}_1 \mathbf{u}_{k+1}\|_2 \leq \sqrt{\frac{1}{\rho_k^{\mathbf{t}}}} \|\mathbf{A} \mathbf{u}_1 - \mathbf{v}\|_2 + \sqrt{\frac{2\tilde{C}k}{\rho_k^{\mathbf{t}}}}, \quad (14)$$

$$\|\mathbf{z}_{k+1} - \mathbf{L}_2 \mathbf{u}_{k+1}\|_2 \leq \sqrt{\frac{1}{\rho_k^{\mathbf{z}}}} \|\mathbf{A} \mathbf{u}_1 - \mathbf{v}\|_2 + \sqrt{\frac{2\tilde{C}k}{\rho_k^{\mathbf{z}}}}. \quad (15)$$

We now prove that the sequences  $(\mathbf{t}_k)_{k=1}^{+\infty}$  and  $(\mathbf{z}_k)_{k=1}^{+\infty}$  are Cauchy sequences. Starting from the expressions of  $\mathbf{t}_{k+1}$  and  $\mathbf{z}_{k+1}$  in Algorithm 2, applying the definition of bounded denoiser and the estimates (14) and (15) the following inequalities hold:

$$\begin{aligned} \|\mathbf{t}_{k+1} - \mathbf{t}_k\|_2 &\leq \|\mathcal{D}_{\sigma_k}^{\text{ext}}(\mathbf{L}_1 \mathbf{u}_k) - \mathbf{L}_1 \mathbf{u}_k\|_2 + \|\mathbf{L}_1 \mathbf{u}_k - \mathbf{t}_k\|_2 \leq \\ &\leq \sqrt{\frac{\alpha}{\rho_k^{\mathbf{t}}}} \sqrt{C_{\mathcal{D}^{\text{ext}}}} + \sqrt{\frac{1}{\rho_{k-1}^{\mathbf{t}}}} \|\mathbf{A} \mathbf{u}_1 - \mathbf{v}\|_2 + \sqrt{\frac{2\tilde{C}(k-1)}{\rho_{k-1}^{\mathbf{t}}}} \end{aligned} \quad (16)$$

$$\begin{aligned} \|\mathbf{z}_{k+1} - \mathbf{z}_k\|_2 &\leq \|\mathcal{D}_{\gamma_k}^{\text{int}}(\mathbf{L}_2 \mathbf{u}_k) - \mathbf{L}_2 \mathbf{u}_k\|_2 + \|\mathbf{L}_2 \mathbf{u}_k - \mathbf{z}_k\|_2 \leq \\ &\leq \sqrt{\frac{\beta}{\rho_k^{\mathbf{z}}}} \sqrt{C_{\mathcal{D}^{\text{int}}}} + \sqrt{\frac{1}{\rho_{k-1}^{\mathbf{z}}}} \|\mathbf{A} \mathbf{u}_1 - \mathbf{v}\|_2 + \sqrt{\frac{2\tilde{C}(k-1)}{\rho_{k-1}^{\mathbf{z}}}}. \end{aligned} \quad (17)$$

By assumption **A.3**  $(\mathbf{z}_k)_{k=1}^{+\infty}$  and  $(\mathbf{t}_k)_{k=1}^{+\infty}$  are Cauchy sequences. Hence, there exist  $\mathbf{t}^*$  and  $\mathbf{z}^*$  such that  $\mathbf{t}_k \rightarrow \mathbf{t}^*$  and  $\mathbf{z}_k \rightarrow \mathbf{z}^*$ .

Furthermore, the following inequalities (which use (14) and (15), respectively) state that  $\mathbf{L}_1 \mathbf{u}_{k+1} \rightarrow \mathbf{t}^*$  and  $\mathbf{L}_2 \mathbf{u}_{k+1} \rightarrow \mathbf{z}^*$ :

$$\|\mathbf{L}_1 \mathbf{u}_{k+1} - \mathbf{t}^*\|_2 \leq \|\mathbf{L}_1 \mathbf{u}_{k+1} - \mathbf{t}_{k+1}\|_2 + \|\mathbf{t}_{k+1} - \mathbf{t}^*\|_2, \quad (18)$$

$$\|\mathbf{L}_2 \mathbf{u}_{k+1} - \mathbf{z}^*\|_2 \leq \|\mathbf{L}_2 \mathbf{u}_{k+1} - \mathbf{z}_{k+1}\|_2 + \|\mathbf{z}_{k+1} - \mathbf{z}^*\|_2. \quad (19)$$

Now, we prove the convergence of the sequence  $(\mathbf{u}_k)_{k=1}^{\infty}$  computed as in Algorithm 2. At step  $k$ ,  $\mathbf{u}_{k+1}$  is the solution of the convex minimization problem (9), therefore the first order optimality conditions lead:

$$\left( \frac{1}{\rho_k^{\mathbf{t}}} \mathbf{A}^T \mathbf{A} + \mathbf{L}_1^T \mathbf{L}_1 + \frac{\rho_k^{\mathbf{z}}}{\rho_k^{\mathbf{t}}} \mathbf{L}_2^T \mathbf{L}_2 \right) \mathbf{u}_{k+1} = \frac{1}{\rho_k^{\mathbf{t}}} \mathbf{A}^T \mathbf{v} + \mathbf{L}_1^T \mathbf{t}_{k+1} + \frac{\rho_k^{\mathbf{z}}}{\rho_k^{\mathbf{t}}} \mathbf{L}_2^T \mathbf{z}_{k+1}. \quad (20)$$

If we define  $\mathbf{M}_k := \frac{1}{\rho_k^{\mathbf{t}}} \mathbf{A}^T \mathbf{A} + \mathbf{L}_1^T \mathbf{L}_1 + \frac{\rho_k^{\mathbf{z}}}{\rho_k^{\mathbf{t}}} \mathbf{L}_2^T \mathbf{L}_2$ , then  $\forall k > 1$ ,  $\mathbf{M}_k$  is invertible for assumption **A.2**. Hence, we can write for each  $k$ :

$$\mathbf{u}_{k+1} = \mathbf{M}_k^{-1} \left( \frac{1}{\rho_k^{\mathbf{t}}} \mathbf{A}^T \mathbf{v} + \mathbf{L}_1^T \mathbf{t}_{k+1} + \frac{\rho_k^{\mathbf{z}}}{\rho_k^{\mathbf{t}}} \mathbf{L}_2^T \mathbf{z}_{k+1} \right). \quad (21)$$

We observe that the two sequences in the right hand side of (21), represented by  $(\mathbf{M}_k^{-1})_{k=1}^{\infty}$  and by the term in parenthesis, are convergent pointwise (by assumption **A.3** and by considering the convergence of the sequences  $(\mathbf{t}_k)_{k=1}^{\infty}$  and  $(\mathbf{z}_k)_{k=1}^{\infty}$ ). By denoting as  $\mathbf{u}^*$  the product of the two limits, we have proved that  $\mathbf{u}_k \rightarrow \mathbf{u}^*$ . This concludes the proof.  $\square$

The fixed-point convergence Theorem 3.1 does not guarantee that the fixed-point  $\mathbf{u}^*$  is a minimum of an implicit defined regularized objective as in (5). However, in the experimental part, we show that the reached fixed-point  $\mathbf{u}^*$  is a good approximation of the desired image  $\mathbf{u}$ .

## 4 The proposed hybrid PnP

In this section we define and motivate the choices of the external and internal denoisers used in our numerical implementation. Moreover, we explain in detail how all the sub-steps in Algorithm 2 can be efficiently performed.

We fix as internal denoiser a scheme based on the Total Variation (TV) [22]. The properties of edge preserving and noise suppressing of the TV in many image processing applications are well-established. The TV function is defined as:

$$\text{TV}(\mathbf{u}) := \sum_{i=1}^n \|(\mathbf{D}\mathbf{u})_i\|_2 = \sum_{i=1}^n \left( \sqrt{(\mathbf{D}_h\mathbf{u})_i^2 + (\mathbf{D}_v\mathbf{u})_i^2} \right), \quad (22)$$

where  $(\mathbf{D}\mathbf{u})_i := ((\mathbf{D}_h\mathbf{u})_i, (\mathbf{D}_v\mathbf{u})_i) \in \mathbb{R}^2$ , for  $i = 1 \dots n$  denotes the discrete image gradient computed at pixel  $i$  along the horizontal and vertical axes, separately. Hence, we can set the function  $g_2$  in (3) as follows:

$$\begin{aligned} g_2 : \mathbb{R}^{2 \times n} &\rightarrow \mathbb{R} \\ \mathbf{x} &\rightarrow \sum_{i=1}^n \|\mathbf{x}_i\|_2 \quad \text{with } \mathbf{x}_i \in \mathbb{R}^2, \end{aligned} \quad (23)$$

and the  $L_2$  operator is the discrete gradient  $\mathbf{D} = (\mathbf{D}_h; \mathbf{D}_v)$  such that  $\mathbf{D}_h, \mathbf{D}_v \in \mathbb{R}^{n \times n}$  are the first order derivative operators along the horizontal and vertical axes, respectively.

We remark that  $g_2$  in (23), through its proximal map, specifies a bounded denoiser.

**Proposition 4.1.** *The proximal map of  $g_2$  is a bounded denoiser according to the Definition 3.1.*

*Proof.* Let us consider  $\mathbf{x} \in \mathbb{R}^{2 \times n}$  and a scalar  $\gamma > 0$ . By (23),  $g_2$  is separable. In the following we refer to  $\mathbf{x}_i \in \mathbb{R}^2$  as the  $i$ -th column of  $\mathbf{x}$ . In [7, 1], the following equality has been proved for  $i = 1 \dots n$ :

$$\begin{aligned} \text{prox}_{g_2, \gamma}(\mathbf{x}) &= (\text{prox}_{\|\cdot\|_2, \gamma}(\mathbf{x}_i))_{i=1 \dots n} \\ \text{where } \text{prox}_{\|\cdot\|_2, \gamma}(\mathbf{x}_i) &= \left( 1 - \frac{\gamma}{\max\{\|\mathbf{x}_i\|_2, \gamma\}} \right) \mathbf{x}_i. \end{aligned}$$

It holds:

$$\begin{aligned} &\|\text{prox}_{\|\cdot\|_2, \gamma}(\mathbf{x}_i) - \mathbf{x}_i\|_2 \leq \\ &\leq \left\| \left( 1 - \frac{\gamma}{\max\{\|\mathbf{x}_i\|_2, \gamma\}} \right) \mathbf{x}_i - \mathbf{x}_i \right\|_2 = \left\| \frac{\gamma}{\max\{\|\mathbf{x}_i\|_2, \gamma\}} \mathbf{x}_i \right\|_2 \leq \gamma. \end{aligned}$$

Hence:

$$\|\text{prox}_{g_2, \gamma}(\mathbf{x}) - \mathbf{x}\|_2^2 \leq \sum_{i=1}^n \|\text{prox}_{\|\cdot\|_2, \gamma}(\mathbf{x}_i) - \mathbf{x}_i\|_2^2 \leq n\gamma^2 \quad (24)$$

which concludes the proof.  $\square$

We remark that, in Algorithm 2,  $\mathcal{D}_{\gamma_k}^{\text{int}}$  is the proximal map of  $g_2$  with parameter  $\gamma_k^2 = \frac{\eta}{\rho_k^2}$ .

Concerning the choice of the external denoiser, due to the state-of-the-art performances in denoising tasks reached by deep learning strategies [29, 4], we embed a Deep CNN denoiser  $\mathcal{D}_\sigma^{\text{CNN}}$  in our Algorithm 2 as  $\mathcal{D}_\sigma^{\text{ext}}$ . Previous studies have already inspected a CNN-based PnP successfully [32, 17] whose CNN denoisers act directly only on the image-domain. Conversely, our denoiser acts on the image through an operator  $\mathbf{L}_1$ , which we set either equal to the identity matrix  $\mathbf{I}$  or the discrete derivative  $\mathbf{D}$ . We will explain in 4.1 how we have implemented the action of the CNN by the operator  $\mathbf{L}_1$ .

The method obtained with the described choices of CNN as external denoiser and TV functional as internal denoiser is reported in Algorithm 3. In the following, we will denote it as I-PnPTV or G-PnPTV when  $\mathbf{L}_1 = \mathbf{I}$  or  $\mathbf{L}_1 = \mathbf{D}$ , respectively.

Since in the numerical experiments we will consider the case where only the external CNN denoiser is plugged in (thus excluding the internal prior), we report for completeness Algorithm 4. Coherently, we label this scheme as I-PnP or G-PnP when  $\mathbf{L}_1 = \mathbf{I}$  or  $\mathbf{L}_1 = \mathbf{D}$ , respectively. We stress that I-PnP is equal to the approach proposed in [32] and there named as IRCNN.

---

**Algorithm 3**  $L_1$ -PnPTV
 

---

**Input:**  $\alpha, \beta$  and  $(\rho_k^t)_{k=1}^\infty, (\rho_k^z)_{k=1}^\infty, \mathbf{A}, \mathbf{L}_1, \mathbf{v}, \mathbf{u}^1$   
**while** Not Converge **do**  
 $\mathbf{t}_{k+1} = \mathcal{D}_{\sigma_k}^{\text{CNN}}(\mathbf{L}_1 \mathbf{u}_k)$   
 $\mathbf{z}_{k+1} = \arg \min_{\mathbf{z} \in \mathbb{R}^{2 \times n}} \left\{ \eta \sum_{i=1}^n \left\{ \|\mathbf{z}_i\|_2 + \frac{\rho_k^z}{2} \|\mathbf{z}_i - (\mathbf{D}\mathbf{u}_k)_i\|_2^2 \right\} \right\}$   
 $\mathbf{u}_{k+1} = \arg \min_{\mathbf{u}} \left\{ \frac{1}{2} \|\mathbf{A}\mathbf{u} - \mathbf{v}\|_2^2 + \frac{\rho_k^t}{2} \|\mathbf{L}_1 \mathbf{u} - \mathbf{t}_{k+1}\|_2^2 + \frac{\rho_k^z}{2} \|\mathbf{D}\mathbf{u} - \mathbf{z}_{k+1}\|_2^2 \right\}$   
**end while**

---

**Algorithm 4**  $L_1$ -PnP
 

---

**Input:**  $\alpha$  and  $(\rho_k^t)_{k=1}^\infty, \mathbf{A}, \mathbf{L}_1, \mathbf{v}, \mathbf{u}^1$   
**while** Not Converge **do**  
 $\mathbf{t}_{k+1} = \mathcal{D}_{\sigma_k}^{\text{CNN}}(\mathbf{L}_1 \mathbf{u}_k)$   
 $\mathbf{u}_{k+1} = \arg \min_{\mathbf{u}} \left\{ \frac{1}{2} \|\mathbf{A}\mathbf{u} - \mathbf{v}\|_2^2 + \frac{\rho_k^t}{2} \|\mathbf{L}_1 \mathbf{u} - \mathbf{t}_{k+1}\|_2^2 \right\}$   
**end while**

---

#### 4.1 Implementation notes

We now refer to particular implementation choices when the previous Algorithms are applied to image deblur, as considered in our numerical experiments. The minimization problem arising, at each step  $k$ , in Algorithms 3 and 4 to compute  $\mathbf{u}_{k+1}$  is solved by applying the first order optimality conditions leading to the following linear system:

$$(\mathbf{A}^T \mathbf{A} + \rho_k^t \mathbf{L}_1^T \mathbf{L}_1 + \rho_k^z \mathbf{D}^T \mathbf{D}) \mathbf{u}_{k+1} = \mathbf{A}^T \mathbf{v} + \rho_k^t \mathbf{L}_1^T \mathbf{t}_{k+1} + \rho_k^z \mathbf{D}^T \mathbf{z}_{k+1}. \quad (25)$$

The matrix  $\mathbf{A}$  is the Toeplitz matrix corresponding to the discrete two dimensional convolution with a specific Point Spread Function (PSF). If we assume periodic boundary conditions, all the previous linear operators are diagonalized by the Fourier Transform and the linear system (25) can be efficiently solved by using the Fast Fourier Transform [10]. Concerning the update of  $\mathbf{z}_k$  in Algorithm 3, we observe that it reduces to the solution of  $n$  bi-dimensional optimization problems which can be computed in a closed form by using the proximal map of the  $L_2$ -norm.

To implement the CNN based external denoiser  $\mathcal{D}_{\sigma}^{\text{CNN}}$  we adopt the widely used DnCNN architecture proposed in [32] and depicted in Figure 1. It is constituted by seven dilated convolutional layers [30] activated by ReLu functions. We consider for the CNN training the *Train400* image dataset [6], also used in [32]. It contains 400 gray-scale natural images of size  $180 \times 180$  obtained by cropping larger images in the Berkeley Segmentation dataset [16]. The training phase of the network depends on the setting of  $\mathbf{L}_1$  which defines the image domain where the noise should be removed. In particular when we set  $\mathbf{L}_1 = \mathbf{I}$ , the CNN denoiser is trained on noisy images (Figure 2a) and we make use of the 25 denoisers downloaded from <https://github.com/cszn/IRCNN>, each one trained on a single noise level in the range [2, 50]. In the case  $\mathbf{L}_1 = \mathbf{D}$  the CNN is trained on  $40 \times 40$  patches of the horizontal gradient images (Figure 2b) on the same 25 noise levels, using the ADAM optimizer and setting the epochs number to 150. The correspondence between the iteration  $k$  of the algorithms and one of the 25 available networks is performed as in [32].

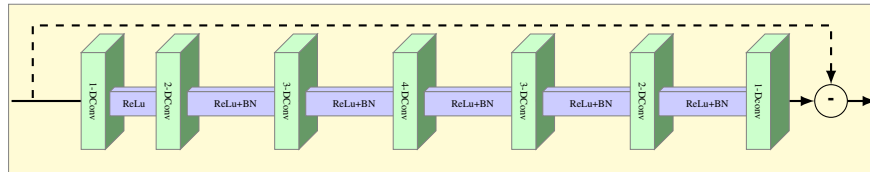


Figure 1: DnCNN architecture scheme. BN represents the batch normalization and  $m$ -DConv denotes  $m$ -dilated convolution.

## 5 Experiments on image denoising and deblurring

In this section, we validate the considered I-PnP, G-PnP, I-PnPPTV and G-PnPPTV schemes on the task of image denoising and deblurring. The Python codes are available at <https://github.com/sedaboni/PnP-TV>. We also compare the baseline TV regularization implemented in the standard ADMM algorithm which uses the discrepancy principle



Figure 2: Image denoising performed by the DnCNN with different choices of the  $L_1$  operator.

[18] for the estimation of the regularization parameter. For this image restoration task, we develop some numerical simulations to discuss the convergence behaviour of the proposed PnP strategies and to compare the results achievable on different kind of images, to highlight the benefits of combining internal and external priors in a unique framework.

For a quality assessment of the results, we compute the Peak Signal-to-Noise-Ratio (PSNR) between the restored image  $\mathbf{u}^*$  and the desired  $\mathbf{u}$ :

$$\text{PSNR}(\mathbf{u}, \mathbf{u}^*) = 10 \log \left( \frac{n^2 \max \mathbf{u}^2}{\|\mathbf{u} - \mathbf{u}^*\|_2^2} \right). \quad (26)$$

To evaluate the noise removal, we compute the standard deviation on uniform regions of interest of the restored images.

For all the proposed algorithms, the input parameters  $\alpha$  and  $\beta$  are heuristically chosen to maximize the PSNR metric at their best in 100 iterations whereas the iterate  $\mathbf{u}^1$  is initialized as a vector of zeros. Concerning the choice of  $(\rho_k^t)_{k=1}^\infty$  and  $(\rho_k^z)_{k=1}^\infty$ , we remark that according to Theorem 3.1 the sequences must be chosen to fulfill the assumption **A.3**. For instance, this holds when  $\rho_k^t = \rho_k^z = k(1 + \epsilon)^k$ , with  $\epsilon > 0$ .

### 5.1 Results on a test problem

We start our experiments by considering the numerical simulation acting on the gray-scale  $512 \times 512$  image reported in Figure 3a. The image is designed to test the algorithms performance in the case of low and high contrast, curve and straight objects: the ground truth image contains many circles of different diameter but uniform intensity; each row has homogeneous circles, with enhancing contrast with respect to the uniform background from the first to the third row. The fourth row contains crosses of different thickness and higher contrast than the circles with respect to the background. To build our test problems, we blur the ground truth image using a Gaussian  $7 \times 7$  kernel with zero mean and standard deviation 1.2, then we introduce AWGN with standard deviation  $std$  in  $\{2.5, 10, 15, 20\}$ . Figure 3b shows the corrupted image obtained with  $std = 15$  together with two zoomed patches on the biggest upper circle and on the second cross.

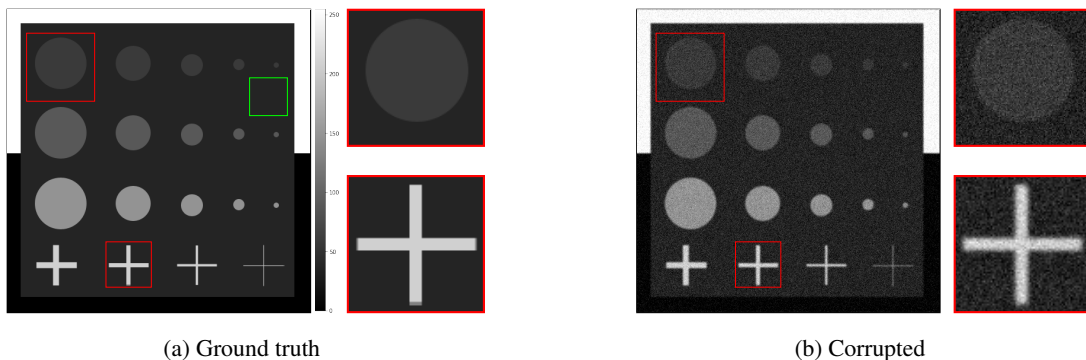


Figure 3: Ground truth gray-scale test image and a simulated degraded acquisition. In (a) and (b) two close-ups (red boxes) are depicted alongside the images. In (a) a gray-scale colormap is drawn.

Before examining the images reconstructed with the proposed methods, we briefly analyse the relative error behaviour of the algorithms on an example case, represented by the previous test image (AWGN  $std = 15$ ). We underline that in the other performed tests, the plots had a very similar behaviour and the following discussion can be similarly applied. In Figure 4, we depict the decreasing behaviour of the error over the performed 100 iterations for I-PnPPTV and G-PnPPTV. In the earlier iterations, the initial decreasing rate of I-PnPPTV curve is higher than the G-PnPPTV one but in the last iterations the two curves get a similar slope. This simple test shows that, even if the fixed-point theorem does not guarantee the convergence to a minimizer of a well defined energy function, the fixed-point we approach has

a relative error smaller than the starting iterate. Moreover, the flat behaviour of both the error curves entails that the algorithms enter in a steady-state. We remark that the small fluctuations are due to the selection of different CNN denoisers among the 25 pre-trained ones.

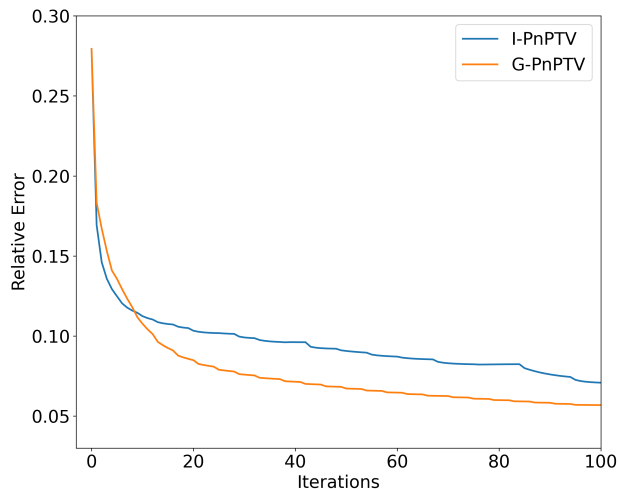


Figure 4: Relative error behaviour along the iterations performed by I-PnP and G-PnP methods.

We now analyse the deblurred images obtained with the proposed PnP schemes. Figure 5 shows the restored images we get from the blurred and noisy image 3b, with the corresponding close-ups. For each reconstruction, we also consider two profiles of interest, created by plotting the intensities of a single image row, in Figures 6 and 7. The former profile is over the lowest-contrasted circles and the latter is over the highest-contrasted ones. For each algorithm, the reconstruction of the corresponding two smallest objects is shown in a zoomed crop, in order to compare objects with severely reduced size.

We first discuss Figure 5. By looking at the low-contrast circle, zoomed in Figure 5, we can see that the noise is present when only the external prior is plugged in (i.e. in I-PnP and G-PnP methods). The introduction of the internal TV-based prior improves the results, by enhancing the circle contour and suppressing the residual noise, as evident in Figure 5c-5d. On the contrary, using only the internal prior induced by the TV reduces too much the contrast between the object and the background, as evident from Figure 5e. Focusing on the bright cross in the last row of Figure 5, we observe that G-PnP and I-PnP restorations obtained with combined external and internal priors improve the quality of the images obtained with only one prior, since they better preserve the edges and the gray-level uniformity of the object.

Through a deeper inspection of Figure 6, we remark that the use of the G-PnP is effective when we focus on small objects with a light contrast to the background. Here, in fact, the I-PnP algorithm does not suppress the noise sufficiently and it creates unwanted artifacts, both inside the circles and in the surrounding background (Figure 6a). The use of the sole gradient-based external prior in G-PnP better restores the intensity of the smallest object but the image is still noisy (Figure 6b), whereas adding the internal prior succeeds in making both sharper boundaries and uniform area (Figure 6d), without being negatively affected by the TV classical loss-of-contrast drawback (Figure 6e).

In Figure 7 we compare the results obtained by G-PnP, G-PnP and TV algorithms on high contrasted objects. Again we note that the external prior, in the G-PnP scheme, well restores the borders of the objects, but do not completely remove the AWGN. Conversely, the use of the TV denoiser causes a loss of contrast. Again, the hybrid scheme provides a good compromise between noise removal and shape and intensities recovering (Figure 7b).

To test the robustness of the proposed models with respect to the noise, we analyze the image enhancements obtained by the considered methods when different variances of the AWGN are considered. The results are reported in Table 1. We observe that, in terms of PSNR, the G-PnP methods gets the best values in all the cases, thus confirming the effectiveness, on this image, of the proposed CNN denoiser defined on the image gradient domain. When we introduce the contribution of the TV-based internal prior, the PSNR values decrease, even if the global denoising effect due to TV is visually evident, as previously underlined.

To confirm this statement, we report in Table 1 the standard deviation (ROI-std) computed on the region having constant values in the original image and marked with a green bounding square in Figure 3a. The TV method has the lowest values because, as already observed, it over-smooths the reconstructions, whereas I-PnP and G-PnP fail in case

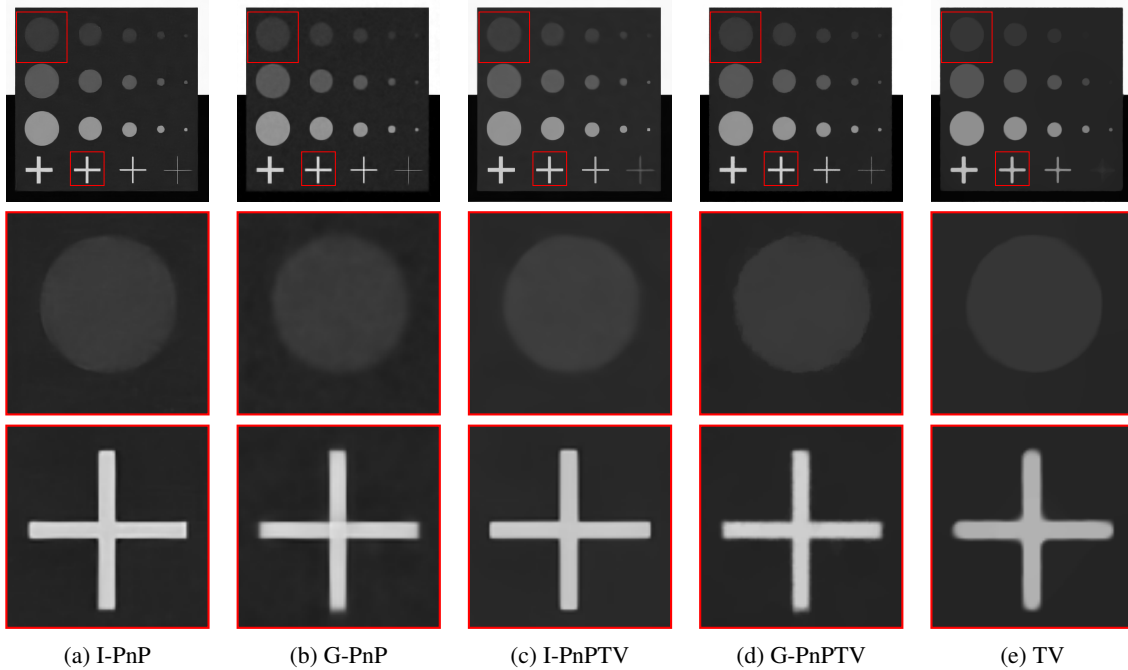


Figure 5: In the first row: image reconstructions by different methods obtained from the acquisition reported in Figure 3b. In the second and in the third rows: two close-ups (x4) underlined by red boxes for each reconstruction.

	AWGN of $std = 2.5$		AWGN of $std = 10$		AWGN of $std = 15$		AWGN of $std = 20$	
	PSNR	ROI-std	PSNR	ROI-std	ROI-PSNR	ROI-std	PSNR	ROI-std
TV	35.4506	<b>0.0290</b>	31.6501	<b>0.0271</b>	29.9166	<b>0.0507</b>	28.5088	<b>0.0772</b>
I-PnP	<b>41.9703</b>	0.5015	<b>40.5462</b>	0.6902	<b>39.3018</b>	0.9848	<b>37.2242</b>	1.2389
I-PnPPTV	39.6786	<b>0.1771</b>	35.0547	0.6841	34.3955	0.6802	33.9578	0.8570
G-PnP	<b>41.9909</b>	0.4046	<b>40.4701</b>	1.1198	<b>39.5992</b>	0.9407	<b>38.7817</b>	1.1838
G-PnPPTV	40.2754	0.5540	36.2615	<b>0.2812</b>	35.3277	<b>0.2470</b>	34.5159	<b>0.3064</b>

Table 1: Measures computed on restored images varying the standard deviation of the AWGN. The two best PSNR and ROI-std (standard deviation computed inside the green square in Figure 3a) values for each AWGN are highlighted in blue and green, respectively. The first best is highlighted in bold.

of high-noise levels. As regards the proposed hybrid methods, these values validate the efficacy of combining internal and external priors.

## 5.2 Results on real medical images

We now consider two X-ray Computed Tomography (CT) images to compare the effectiveness of the proposed schemes. In order to illustrate the action of the proposed image-based and gradient-based external priors we examine a low-contrast image, whereas to display the benefit of internal prior for noise removal we consider a high contrasted image containing flat regions. Both the images are post-processed and still contain little noise. However we further blur them to stress our algorithms on a more realistic test.

We start analysing a low-dose computed tomography (LDCT) chest image and we blur it with a Gaussian PSF with zero mean and standard deviation 0.5. In Figure 8a we show the corrupted image and two zoomed regions characterized by different contrast levels. We examine here the behaviour of external priors applied to different image domains, hence in Figure 8 (b)-(c) we include the reconstructed images given by the I-PnP and G-PnP algorithms and two corresponding regions of interest. In the second row, the close-ups show that I-PnP does not preserve the shapes but it gives a smoother result than G-PnP on sparse and small details. In the third row, the close-ups show I-PnP and G-PnP recover quite well the object shapes but the former introduces some noisy artifacts which are not present in reconstruction obtained with the CNN-based gradient denoisers. The small details on the dark background are almost completely suppressed by I-PnP. On the contrary, G-PnP preserves these components but it also introduces an unwanted blurry effect. We

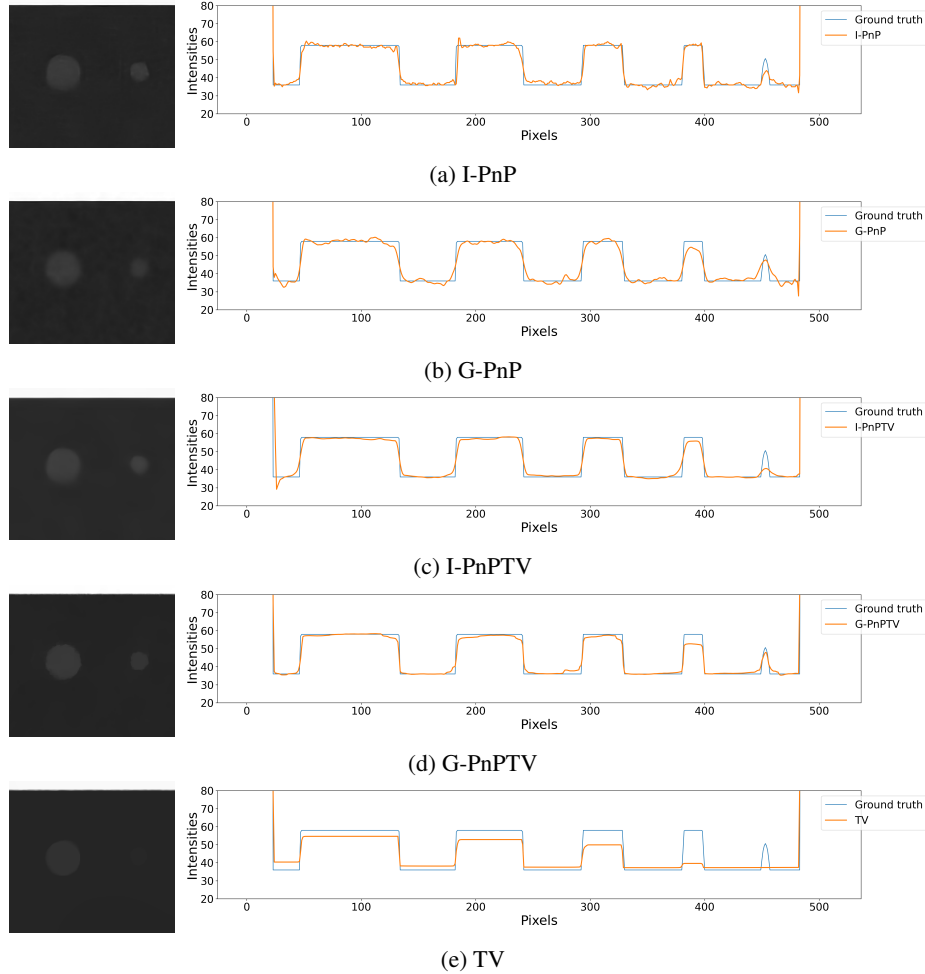


Figure 6: Intensity line profiles on the 90th row cutting the lowest contrasted circles. The blue and orange lines represent the ground truth and the restored image profiles for different methods, respectively.

	Starting	I-PnP	G-PnP	I-PnP+TV	G-PnP+TV	TV
ROI-std	15.007	2.348	2.552	1.049	1.162	0.024

Table 2: Standard deviation computed on the region of interest inside the green square in Figure 8a, for the LDCT chest images.

can conclude that the use of gradient-based CNN denoiser has some advantages with respect to an image-based CNN denoiser in preserving small details of the image. To measure the noise on the reconstruction, we computed the standard deviation inside the region defined by the green square in Figure 8a and we reported them in Table 2. These metrics are similar for both I-PnP and G-PnP, whereas the contribution of TV for the internal prior generates lower standard deviation values for both I-PnP+TV and G-PnP+TV.

We now take into account a head tomographic image. We corrupt the original image, by blurring it with a Gaussian  $7 \times 7$  PSF with zero mean and standard deviation 1.2. The resulting image is shown in Figure 9a. In Figure 9b and 9c we also depict the denoised and deblurred images given by G-PnP and G-PnP+TV algorithms. It is evident that G-PnP+TV suppresses the noisy artifacts visible in the G-PnP restored image. In Figure 10 we zoom over two different regions of the reconstructions obtained using the four proposed methods. The former close-up contains high-contrast objects whereas the latter comprises a low-contrast area inside the three white vertebral patches and a darker region. The denoising effects achieved by the I-PnP and G-PnP methods are limited but shape recovery results are remarkable. The I-PnP+TV algorithm better removes the noise, however it also suppresses details inside the central low-contrast area and the image appears quite flat. At last, the G-PnP+TV method better balances and mixes the effects of the learned

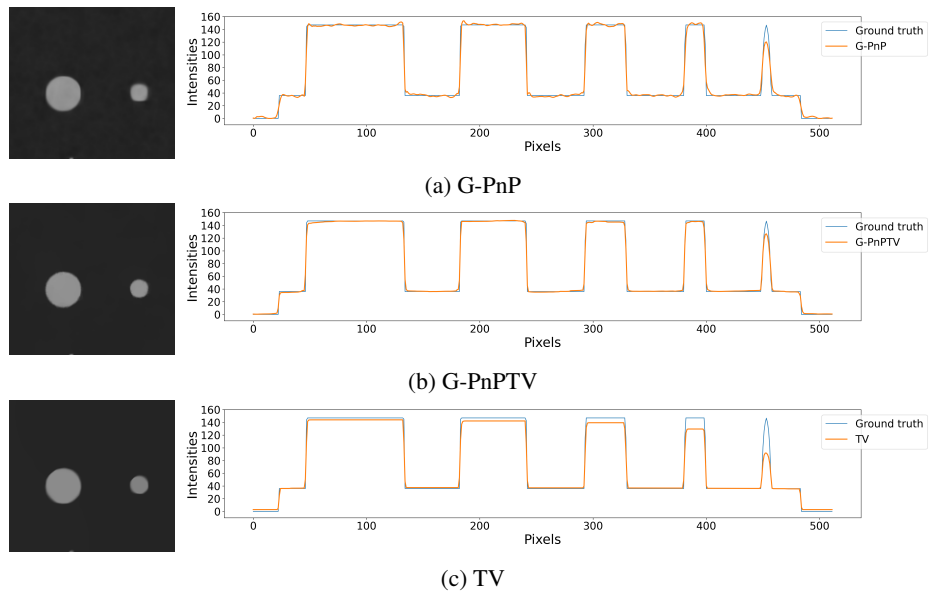


Figure 7: Intensity line profiles on the 370th row cutting the highest contrast circles. The blue and orange lines represent the ground truth and the restored image profiles for different methods, respectively.

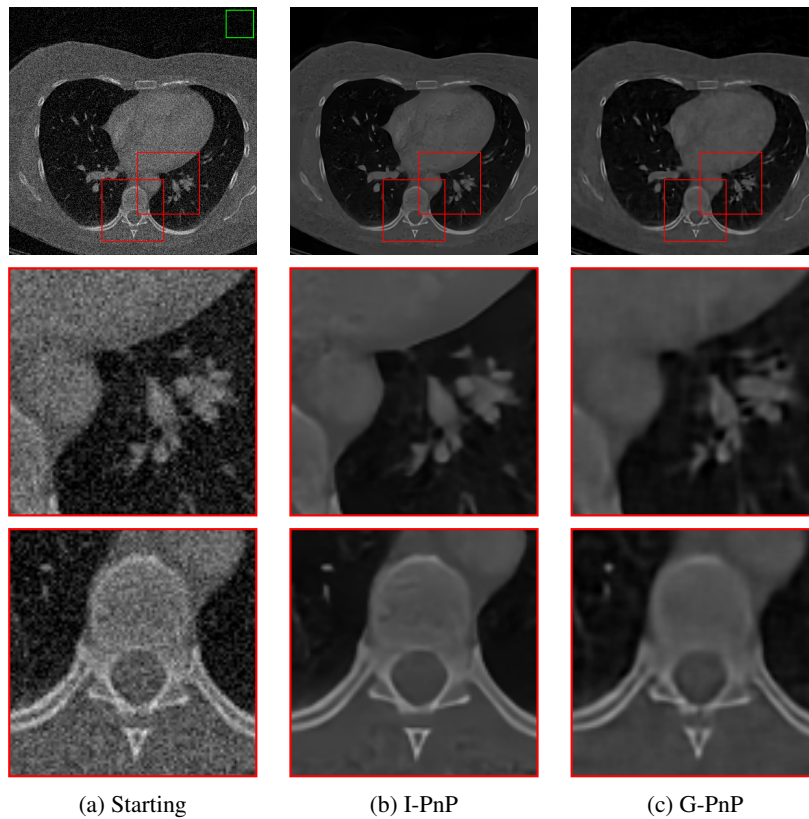


Figure 8: In the first row: noisy and blurred acquisition of the LDCT chest image alongside reconstructions by different methods. In the second and in the third rows: two close-ups (x4) underlined by red boxes.

	Starting	I-PnP	G-PnP	I-PnPPTV	G-PnPPTV	TV
ROI-std	15.016	2.350	2.803	0.967	1.896	0.059

Table 3: Standard deviation computed on the region of interest defined by the green square in 9a, for the head CT image.

denoiser with the TV edge preserving capability and it leads to a visually enhanced reconstruction. In Table 3 we report the standard deviation computed on the uniform patch inside the green square in Figure 9. The over-smoothing effect of I-PnPPTV and G-PnPPTV is validated by the value of standard deviation on the region of interest, which are largely lower than the ones computed on I-PnP and G-PnP reconstructions, respectively, thus confirming that the TV internal prior enhances the reconstructions quality in terms of noise suppression.



Figure 9: Noisy and blurred acquisition of the head CT image alongside two different reconstructions.

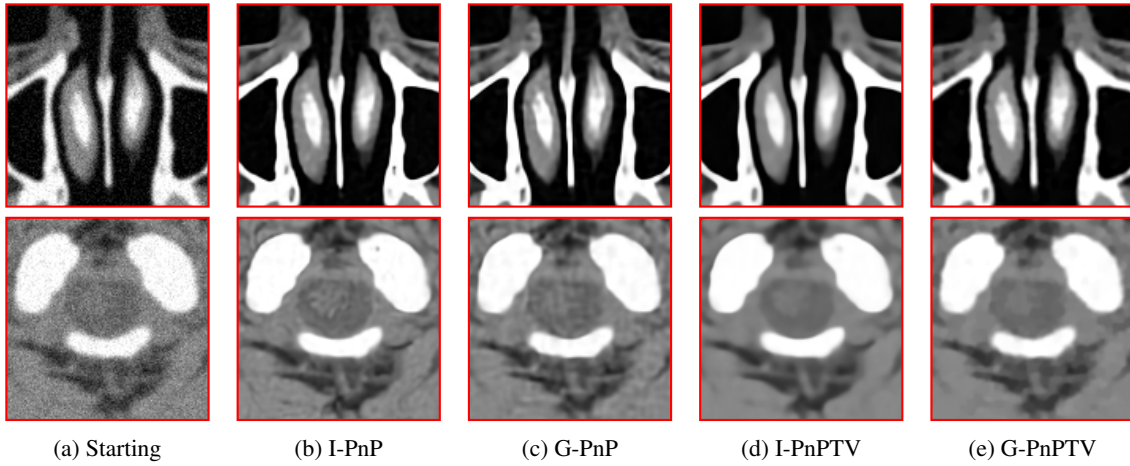


Figure 10: Close-ups (x4) of the noisy and blurred acquisition of the head CT image alongside the reconstructions by different methods.

## 6 Conclusions

In this paper we have presented a new flexible Plug-and-Play framework based on a Half-Quadratic Splitting algorithm, which has its strength in combining both internal and external priors specified by suitable denoisers. Moreover by considering an external denoiser acting on a specific image domain, such as the gradient one, we have introduced a generalization on the external prior which will merit further investigations. We have endowed our novel hybrid PnP

with a fixed-point convergence theorem upon weak assumptions on the involved denoisers. In our implementation, the external denoiser is chosen as a CNN, trained on noisy images or gradients, whereas the internal denoiser arises from Total Variation regularization. We have obtained very promising results for deblurring and denoising experiments performed on images characterized by sparse gradients. The external priors well recover the shapes of the objects, especially in the case of curve contours and low-contrast images; the proposed gradient-based CNN denoiser outperforms the image-based CNN denoiser in the reconstruction of flat areas and small homogeneous objects in a uniform background, as in the case of the head CT image. However, the measures of standard deviation in flat regions are quite high, confirming that the noise has not been fully removed. The use of the sole TV regularization oversmooths the reconstructions creating loss-of-contrast drawbacks and staircase effects. However, combining external and internal priors produces better results in all the performed experiments. We remark that different bounded internal and external denoisers, chosen according to the characteristics of the images, can be employed in the proposed PnP framework in place of the considered ones, maintaining the convergence properties proved. A deeper insight on the choice of the CNN architecture and on its training will be subject of future work, to improve the overall performances of the proposed schemes.

## Acknowledgments

This research was funded by the Indam GNCS grant 2020 *Ottimizzazione per l'apprendimento automatico e apprendimento automatico per l'ottimizzazione*.

## References

- [1] Amir Beck. First-order methods in optimization. *SIAM*, 2017.
- [2] Mario Bertero. Introduction to inverse problems in imaging. *CRC press*, 2020.
- [3] Antoni Buades, Bartomeu Coll, and J-M Morel. A non-local algorithm for image denoising. In 2005 IEEE Computer Society Conference on Computer Vision and Pattern Recognition (CVPR'05), volume 2, pages 60–65. *IEEE*, 2005.
- [4] Harold C Burger, Christian J Schuler, and Stefan Harmeling. Image denoising: Can plain neural networks compete with BM3D? In 2012 IEEE conference on computer vision and pattern recognition, pages 2392–2399. *IEEE*, 2012.
- [5] Stanley H Chan, Xiran Wang, and Omar A Elgendy. Plug-and-play ADMM for image restoration: Fixed-point convergence and applications. *IEEE Transactions on Computational Imaging*, 3(1):84–98, 2016.
- [6] Yunjin Chen and Thomas Pock. Trainable nonlinear reaction diffusion: A flexible framework for fast and effective image restoration. *IEEE transactions on pattern analysis and machine intelligence*, 39(6):1256–1272, 2016.
- [7] Patrick L Combettes and Jean-Christophe Pesquet. Proximal splitting methods in signal processing. In Fixed-point algorithms for inverse problems in science and engineering, pages 185–212. *Springer*, 2011.
- [8] Kostadin Dabov, Alessandro Foi, Vladimir Katkovnik, and Karen Egiazarian. Image denoising by sparse 3-D transform-domain collaborative filtering. *IEEE Transactions on image processing*, 16(8):2080–2095, 2007.
- [9] Donald Geman and Chengda Yang. Nonlinear image recovery with half-quadratic regularization. *IEEE transactions on Image Processing*, 4(7):932–946, 1995.
- [10] Per Christian Hansen, James G Nagy, Dianne P Leary, and Rodney Miller. Deblurring images: Matrices, spectra and filtering. *Journal of Electronic Imaging*, 17(1):019901–019901, 2008.
- [11] Ulugbek S Kamilov, Hassan Mansour, and Brendt Wohlberg. A plug-and-play priors approach for solving nonlinear imaging inverse problems. *IEEE Signal Processing Letters*, 24(12):1872–1876, 2017.
- [12] Germana Landi and E Loli Piccolomini. An efficient method for nonnegatively constrained Total Variation-based denoising of medical images corrupted by poisson noise. *Computerized Medical Imaging and Graphics*, 36(1):38–46, 2012.
- [13] Bei Li and DaShun Que. Medical images denoising based on total variation algorithm. *Procedia Environmental Sciences*, 8:227–234, 2011.
- [14] Housen Li, Johannes Schwab, Stephan Antholzer, and Markus Haltmeier. *NETT: Solving inverse problems with deep neural networks*. Inverse Problems, 2020.
- [15] Sebastian Lutz, Ozan Öktem, and Carola-Bibiane Schönlieb. Adversarial regularizers in inverse problems. In *Advances in Neural Information Processing Systems*, pages 8507–8516, 2018.

- [16] D. Martin, C. Fowlkes, D. Tal, and J. Malik. *A Database of Human Segmented Natural Images and its application to evaluating segmentation algorithms and measuring ecological statistics*. In Proc. 8th Int'l Conf. Computer Vision, volume 2, pages 416–423, July 2001.
- [17] Tim Meinhardt, Michael Moller, Caner Hazirbas, and Daniel Cremers. *Learning proximal operators: Using denoising networks for regularizing inverse imaging problems*. In Proceedings of the IEEE International Conference on Computer Vision, pages 1781–1790, 2017.
- [18] Vladimir Alekseevich Morozov. *Methods for solving incorrectly posed problems*. Springer, 1984.
- [19] Inbar Mosseri, Maria Zontak, and Michal Irani. *Combining the power of internal and external denoising*. In IEEE international conference on computational photography (ICCP), pages 1–9. IEEE, 2013.
- [20] Jorge Nocedal and Stephen Wright. *Numerical optimization*. Springer Science & Business Media, 2006.
- [21] Shunsuke Ono. *Primal-dual plug-and-play image restoration*. IEEE Signal Processing Letters, 24(8):1108–1112, 2017.
- [22] Leonid I Rudin, Stanley Osher, and Emad Fatemi. *Nonlinear total variation based noise removal algorithms*. Physica D: nonlinear phenomena, 60(1-4):259–268, 1992.
- [23] Ernest Ryu, Jialin Liu, Sicheng Wang, Xiaohan Chen, Zhangyang Wang, and Wotao Yin. *Plug-and-Play Methods Provably Converge with Properly Trained Denoisers*. Proceedings of Machine Learning Research, 2019.
- [24] Suhas Sreehari, S Venkat Venkatakrishnan, Brendt Wohlberg, Gregory T Buzzard, Lawrence F Drummy, Jeffrey P Simmons, and Charles A Bouman. *Plug-and-play priors for bright field electron tomography and sparse interpolation*. IEEE Transactions on Computational Imaging, 2(4):408–423, 2016.
- [25] Yu Sun, Brendt Wohlberg, and Ulugbek S Kamilov. *An online plug-and-play algorithm for regularized image reconstruction*. IEEE Transactions on Computational Imaging, 5(3):395–408, 2019.
- [26] Afonso M Teodoro, José M Bioucas-Dias, and Mário AT Figueiredo. *Scene-adapted plug-and-play algorithm with convergence guarantees*. In 2017 IEEE 27th International Workshop on Machine Learning for Signal Processing (MLSP), pages 1–6. IEEE, 2017.
- [27] Singanallur V Venkatakrishnan, Charles A Bouman, and Brendt Wohlberg. *Plug-and-play priors for model based reconstruction*. In 2013 IEEE Global Conference on Signal and Information Processing, pages 945–948. IEEE, 2013.
- [28] Yilun Wang, Junfeng Yang, Wotao Yin, and Yin Zhang. *A new alternating minimization algorithm for total variation image reconstruction*. SIAM Journal on Imaging Sciences, 1(3):248–272, 2008.
- [29] Junyuan Xie, Linli Xu, and Enhong Chen. *Image denoising and inpainting with deep neural networks*. In Advances in neural information processing systems, pages 341–349, 2012.
- [30] Fisher Yu and Vladlen Koltun. *Multi-scale context aggregation by dilated convolutions*. arXiv preprint arXiv:1511.07122, 2015.
- [31] Kai Zhang, Yawei Li, Wangmeng Zuo, Lei Zhang, Luc Van Gool, and Radu Timofte. *Plug-and-play image restoration with Deep Denoiser Prior*. arXiv preprint, 2020.
- [32] Kai Zhang, Wangmeng Zuo, Shuhang Gu, and Lei Zhang. *Learning deep CNN denoiser prior for image restoration*. In Proceedings of the IEEE conference on computer vision and pattern recognition, pages 3929–3938, 2017.
- [33] Kai Zhang, Wangmeng Zuo, and Lei Zhang. *Deep plug-and-play super-resolution for arbitrary blur kernels*. In Proceedings of the IEEE Conference on Computer Vision and Pattern Recognition, pages 1671–1681, 2019.
- [34] Daniel Zoran and Yair Weiss. *From learning models of natural image patches to whole image restoration*. In 2011 International Conference on Computer Vision, pages 479–486. IEEE, 2011.